Microscale Descriptors for Particle-Void Distribution and Jamming Transition in Pre- and Post-Liquefaction of Granular Soils

Jiangtao Wei[1]; Duruo Huang[2]; and Gang Wang, M.ASCE[3]

Abstract: Micromechanical modeling provides significant insight into the fundamental mechanism of soil liquefaction. In this study, a series of undrained cyclic simple shear simulations were conducted by using discrete element method (DEM). The particle-scale information provided by DEM was used to quantify the local void distribution around particles. Two microscale descriptors, named as the shape-elongation descriptor (E_d) and the orientation-anisotropy descriptor (A_d), were proposed to quantify the overall anisotropy of local void distribution in the granular packing. Before initial liquefaction, the particle-void distribution remains to be globally isotropic for isotropically consolidated samples. An irreversible development of anisotropy in terms of E_d and A_d mainly occurs in the post-liquefaction stage. In addition, jamming transition of the liquefied soil is determined by using these descriptors because a unique hardening state line (HSL) is found in the $E_d - A_d$ space that can differentiate a post-liquefaction flow state from a hardening or jamming state. Furthermore, large post-liquefaction flow strains are found to be closely correlated to the descriptors. **DOI: 10.1061/(ASCE)EM.1943-7889.0001482.** © 2018 American Society of Civil Engineers.

Author keywords: Discrete-element method; Liquefaction; Particle-void structure; Jamming transition.

Introduction

For saturated soils under undrained cyclic loading, cyclic mobility and flow liquefaction may induce large ground deformation and cause severe damage to civil structures. Initial liquefaction refers to the first time when effective confining stress decreases to zero and excess pore water pressure ratio increases to 100% (Seed and Lee 1966). The overall undrained cyclic loading process can be separated into pre- and post-liquefaction stages by the initial liquefaction. In the post-liquefaction stage, granular soils would experience large flow deformation in a "fluid-like" state under nearly zero effective stress (Idriss and Boulanger 2008). Jamming transition could occur in the liquefied soil, leading to a hardening state or *solid-like* state under nonzero effective stress (Shamoto et al. 1997).

Although the geotechnical community has long known that cyclic liquefaction and cyclic mobility result in significant changes in the load-bearing fabric of the granular soil, a clear characterization of these changes has been lacking. Here, fabric of granular soils refers to the arrangement of particles, particle group, and void space distribution (Mitchell and Soga 2005). It has been found that the fabric has a profound influence on the properties of sands such as the small-strain stiffness, permeability, peak strength, and dilatancy (Sitar 1983; Wang and Mok 2008; Ventouras and Coop 2009; Fonseca et al. 2012). Exploring the characteristics of fabric will also help to develop physically based constitutive models (Dafalias and Manzari 2004; Zhang and Zhang 2008; Chang and Yin 2010; Yin et al. 2010; Wang and Xie 2014; Gao and Zhao 2015; Yin et al. 2017). To quantitatively study the fabric, two-dimensional (2D) biaxial tests using photoelastic disks (Oda et al. 1985) and rods (O'Sullivan et al. 2002) had been conducted. Most recently, a microcomputed tomography (micro-CT) scan technique has been used to get the microscale images of fabric in granular assemblage of real sands (Fonseca et al. 2012).

Yet these technologies have not been implemented in the study of cyclic soil liquefaction. On the other hand, numerical simulations based on discrete element method (DEM) provide a more convenient and less costly choice to observe the fabric directly (Rothenburg and Bathurst 1989; Thornton 2000; O'Sullivan 2011; Guo and Zhao 2013). The DEM has been proven to be capable to investigate the cyclic soil behavior (Ng and Dobry 1994; Sitharam et al. 2009; Phusing and Suzuki 2015). Most recently, DEM has been used successfully to study fabric evolution in the cyclic liquefaction process (Wang and Wei 2016; Wei and Wang 2016, 2017).

Traditional studies on fabric quantification are mostly based on interparticle contact methods (Satake 1992; Kuhn 1999; Thornton 2000; Li and Li 2009; Guo and Zhao 2013), which are easy to implement in the DEM simulation. However, fabric quantification of liquefied soils is particularly challenging because a liquefied soil loses nearly all contact points, so the contact-based fabric may not be a reliable indicator for such a case. On the other hand, void-based fabric can be an option to study cyclic liquefaction. Among very limited studies, a few void-based fabrics have been proposed, including the *void cells* (Satake 1992; Kuhn 1999) and *solid/ void cell system* (Li and Li 2009). However, the construction of the void cell in these studies is still based on either branch vectors (Satake 1992; Kuhn 1999) or interparticle contacts (Li and Li 2009), which is only useful to quantify the anisotropy of void in a solid-like state, but not the *fluid-like* state (Wei and Wang 2015a, b; Wang and Wei 2016). The scan-line method (Oda et al. 1985;

[1]Graduate Student, Dept. of Civil and Environmental Engineering, Hong Kong Univ. of Science and Technology, Clear Water Bay, Kowloon, Hong Kong.

[2]Assistant Professor, Dept. of Hydraulic Engineering, Tsinghua Univ., Beijing 100084, China; Dept. of Civil and Environmental Engineering, Hong Kong Univ. of Science and Technology, Clear Water Bay, Kowloon, Hong Kong (corresponding author). Email: huangdr@ust.hk

[3]Associate Professor, Dept. of Civil and Environmental Engineering, Hong Kong Univ. of Science and Technology, Clear Water Bay, Kowloon, Hong Kong. Email: gwang@ust.hk

Table 1. Loading conditions in the simulation

Sample	Relative density, Dr (%)	CSR
Dr46	46	0.16/0.18/0.20
Dr62	62	0.22/0.25/0.28
Dr74	74	0.30/0.35/0.40

Ghedia and O'Sullivan 2012) is a different approach to quantify void-based fabric. In this method, a 2D image of granular soils is scanned by a series of parallel lines with inclination between −90 and 90°. The void fabric is constructed by the mean length of voids intercepted by the scan lines. This method gives the anisotropy of void-based fabric for granular soils at any state. However, microscale information regarding features of individual voids cannot be captured in the method.

In this paper, a weighted Voronoi tessellation scheme is used to divide the void space around particles without relying on interparticle contact information. Therefore, the method is well suitable for developing void-based fabric for even fully liquefied soils. In this study, two new void-based fabrics, E_d and A_d, are developed to characterize the shape and orientation of local void distribution around particles. The evolution of these new fabric measures is studied for granular soils before and after liquefaction through a series of undrained cyclic simple shear tests conducted using the DEM simulation. Post-liquefaction behaviors, in terms of jamming transition and flow deformation, are correlated to these new descriptors. The microscale study aims at providing insight into the fundamental mechanism of soil liquefaction.

DEM Simulation of Cyclic Behavior

To conduct the numerical simulations, an open-source DEM code, Yade (Šmilauer et al. 2015), is used. A total of 4,000 circular (2D)

particles are randomly generated within a squared representative volume element (RVE). The radius of particles ranges from 0.15 to 0.45 mm, and the mean radius R_{50} is 0.3 mm. The simplified Hertz–Mindlin model (Yimsiri and Soga 2010) is used to describe the interparticle contact behaviors in loading and unloading. All particles have Young's modulus of 70 GPa and Poisson's ratio of 0.3. Note that periodic boundary condition is prescribed on this RVE to enhance the shear strain field to be uniform inside the RVE even when a relatively small number of particles are used.

First, the particles are consolidated isotropically under a confining pressure of 100 kPa, then subjected to undrained cyclic simple shear tests. Table 1 summarizes the loading conditions of the cyclic simple shear tests, in which three samples of different relative densities (Dr = 46, 62, and 72%) are generated. The maximum void ratio, e_{max}, and the minimum void ratio, e_{min}, are determined as 0.272 and 0.178, respectively, based on DEM simulations. It should be noted that "relative density" used in this study is only a nominal terminology to indicate different denseness of the packing, and it does not have the same meaning as that used in the laboratory. The cyclic shear stress ratio (CSR) is defined as the cyclic shear stress (τ) divided by the vertical consolidation stress ($\sigma'_{v,0} = 100$ kPa), such that CSR = $\tau/\sigma'_{v,0}$ (Idriss and Boulanger 2008). The model setup is shown in Fig. 1(a).

Figs. 1(b and c) show that the simulation results of sample Dr62 are qualitatively similar to experimental results (Shamoto et al. 1997). With the increase of cycle numbers, effective vertical stress (σ'_v) gradually decreases until initial liquefaction occurs. The initial liquefaction is based on the occurrence of zero effective vertical stress, in practice, $\sigma'_v < 0.5$ kPa. After liquefaction, the stress path shows repeated *butterfly* loops while the shear strain amplitude keeps increasing cycle by cycle. Within a loading cycle in post-liquefaction stage, granular packing is transformed between a flow state and a hardening state. Accordingly, the shear deformation is
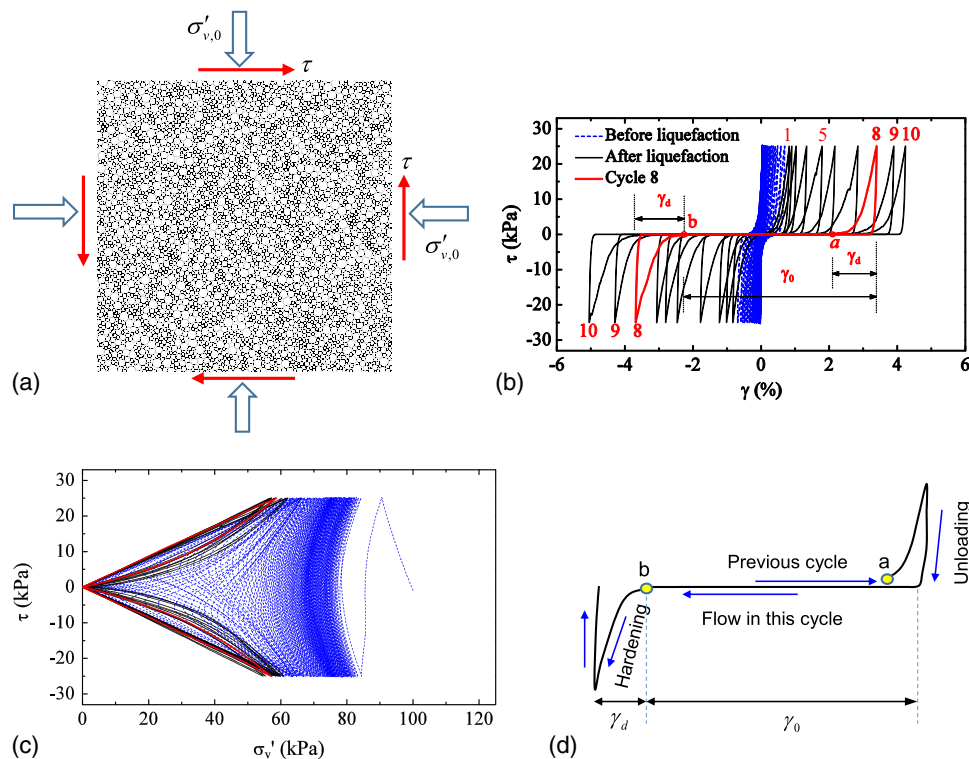
Fig. 1. Cyclic stress-strain behaviors of sample Dr = 62% with CSR = 0.25: (a) model setup; (b) shear stress and strain curve; (c) stress path; and (d) definition of the flow strain and hardening strain. The cycle number is counted from initial liquefaction.

© ASCE

J. Eng. Mech.

divided into flow strain and hardening strain (Shamoto et al. 1997), as shown in Fig. 1(d). The flow strain (γ_0) refers to the double-amplitude strain component when shear stiffness is extremely low and effective stress is almost zero. During flow state, granular packing behaves like a fluid. The hardening strain (γ_d) refers to the strain component when shear stiffness and effective stress have a sharp increase or are much higher than zero. During the hardening state, granular packing behaves like a solid. Note that before initial liquefaction, granular packing belongs to the hardening state. The transition point [Point b in Fig. 1(d)] is the end of the flow strain and the start of the hardening strain. In the hardening state, stress-strain behavior is almost identical between different loading cycles, while flow strain amplitude (γ_0) increases cycle by cycle.

Descriptors for Particle-Void Distribution

Weighted Voronoi Tessellation

In granular packing, particles are trapped in a localized metastable region formed by its surrounding particles (Pouliquen et al. 2003). Particle movement is restricted in the metastable region during shear deformation. In this study, the weighted Voronoi tessellation is used to partition the void space around a particle. Compared with the regular Voronoi tessellation that bisects the distance between centroids of particles, the weighted Voronoi tessellation uses the radius of particles as a weight when dividing the void space, such that a single particle will be entirely encased by a polygonal Voronoi cell, as shown in Fig. 2. Note that if the regular Voronoi tessellation is used, the Voronoi cell may undesirably crosscut multisized particles. Mathematically, the particle and its surrounding void space can be described as $\{P^{(i)}, R^{(i)}, [V_1^{(i)}, \ldots, V_k^{(i)}]\}$, where $P^{(i)}$ is the center of the particle i, $R^{(i)}$ is the radius of the particle i, and $[V_1^{(i)}, \ldots, V_k^{(i)}]$ are vertexes of the Voronoi cell. Note that construction of the Voronoi cell does not rely on interparticle contact information; therefore, it can be well used to study the void distribution in a liquefied granular packing even if particles lose their contact.

Definition of Cell-to-Particle Ratio

The void space within a Voronoi cell is the potential space for the particle to move. For example, around the central particle in Fig. 2, large void space can be found in the upper right and lower left
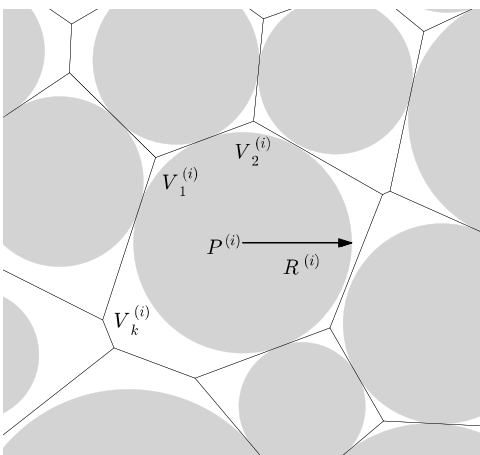
Fig. 2. Weighted Voronoi tessellation of 2D granular packing.

side of the particle. Here, the cell-to-particle ratio (CP ratio) is considered to characterize the local void distribution. The CP ratio is defined as follows:

$$r(\theta) = \frac{R_c(\theta)}{R_p(\theta)} \tag{1}$$

where $R_c(\theta)$ and $R_p(\theta)$ measure the radial dimension of the cell and particle, respectively. $r(\theta)$ describes the angular distribution of the local void around a particle in a cell. Based on the definition, $r(\theta)$ has the following characteristics:

1. There is a clear positive relationship between the enclosed area of $r(\theta)$ and the local void ratio, which is defined as the ratio between area of the void and area of the particle for a cell. For simplicity, if the particle shape is assumed to be circular, i.e., $R_p(\theta) \equiv R_p$, the local void ratio of the cell becomes:

$$e_L = \frac{A_c}{A_p} - 1 = \frac{\oint R_c^2(\theta)d\theta}{\oint R_p^2 d\theta} - 1 = \frac{A_r}{\pi} - 1 \tag{2}$$

   where V_c and V_p = areas of the cell and particle, respectively; and $A_r = \frac{1}{2}\oint r^2(\theta)d\theta$ = enclosed area of $r(\theta)$. Therefore, larger enclosed area of $r(\theta)$ corresponds to higher local void ratio.

2. The shape of $r(\theta)$ reflects anisotropy of local void distribution around a particle. If $r(\theta)$ is elongated [refer to cell No. 1 in Fig. 3(b)], larger void space is distributed along the elongated direction and the compressibility of the cell along the direction would be larger.

Recent studies demonstrated that the probability distribution of e_L remains to be almost constant during an undrained loading (Guo and Zhao 2014), even for the case of large deformation. On the other hand, the anisotropy of local void distribution, i.e., the shape of $r(\theta)$, keeps evolving in undrained cyclic loading, and it may be used as a fabric indicator. In the following section, we will use a Fourier descriptor to analyze the shape of $r(\theta)$.

Fourier Descriptors to Measure Local Anisotropy

Fourier descriptors have been widely used for particle shape characterization (Bowman et al. 2001), which are used to analysis the shape of $r(\theta)$:

$$r^2(\theta) = r_0^2 + \sum_{n=1}^{+\infty} D_n \cos n(\theta - \theta_n) \tag{3}$$

For particle shape characterization, D_2 has been verified to control the particle elongation, and D_3–D_7 control the irregularities of the particle shape (Bowman et al. 2001; Mollon and Zhao 2013). In this study, only elongation and orientation of the shape are considered, so $r(\theta)$ can be approximately expressed as follows:

$$r^2(\theta) = r_0^2 + D_2 \cos 2(\theta - \theta_2) \tag{4}$$

where $r_0^2 = A_r/\pi$; and A_r = enclosed area of $r(\theta)$, such that $\oint r^2(\theta)d\theta/2 = A_r$. Then

$$r^2(\theta) = \frac{A_r}{\pi}[1 + e_d \cos 2(\theta - \theta_d)] \tag{5}$$

where $e_d = \frac{\pi}{A}D_2$ = shape factor of $r(\theta)$ that controls the elongation; and $\theta_d \equiv \theta_2$ = principal orientation of $r(\theta)$. If $e_d = 0$, the shape of $r(\theta)$ is the circle and the principal direction θ_d can be any values. Fig. 3 shows examples of $r(\theta)$ associated with each particle (solid line) and its Fourier approximation (dashed line).

The importance of shape factor (e_d) to mechanical behaviors of granular packing is illustrated in Fig. 4, where two granular
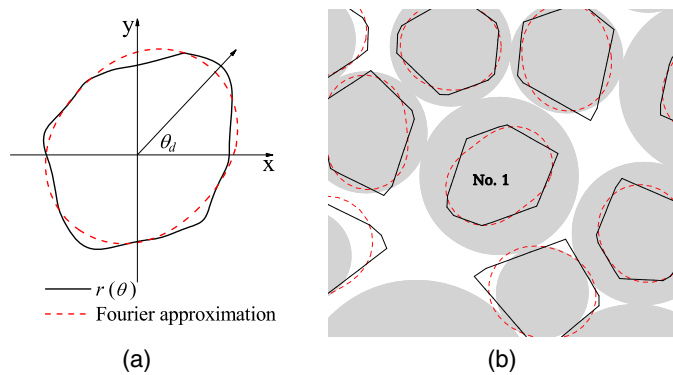
Fig. 3. Fourier approximation of $r(\theta)$.
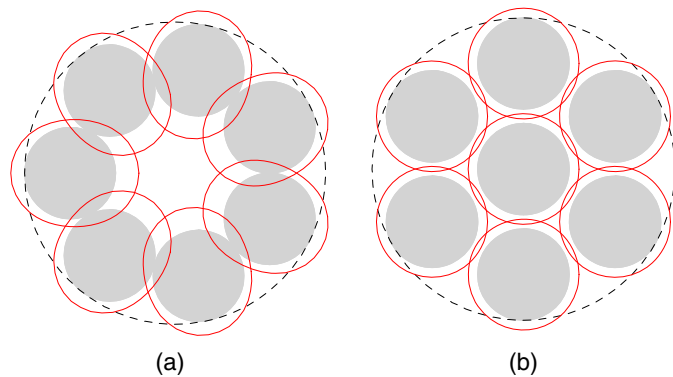
Fig. 4. Granular packings with the same void ratio but different e_d: (a) $e_d = 0.183$; and (b) $e_d = 0$.

packings have different e_d values even though they contain the same amount of particles and void. Particles in Fig. 4(a) form an arching structure ($e_d = 0.183$), and the packing could take loads and behaves like a solid. In Fig. 4(b), particles are separated from each other ($e_d = 0$), and the packing cannot take any load and will behave like a fluid. Note that Fig. 4 is only for illustrative purpose to demonstrate that granular packings with the same void ratio but different e_d can have different mechanical behaviors. It is worth mentioning that some existing fabric indicators would not be able to distinguish these two types of packings clearly. For example, the scan line method (Oda et al. 1985; Ghedia and O'Sullivan 2012) would result in the same void-based fabric that is isotropic for both cases. The *solid/void cell system* (Li and Li 2009) and *void cells* (Satake 1992; Kuhn 1999) will not be applicable to the case of Fig. 4(b), since there is no interparticle contact in the packing.

Quantification of Particle-Void Distribution

The e_d and θ_d in Eq. (5) quantify the local void distribution around a single particle. The e_d measures the shape elongation and the θ_d measures the anisotropy of principal orientation of local void distribution $r(\theta)$. By statistical analysis of $\{e_d, \theta_d\}$ associated with all particles in the granular packing, the particle-void distribution for the entire packing can be quantified.

The first descriptor, named as shape-elongation descriptor E_d, measures the mean value of e_d, and is defined as

$$E_d = \frac{1}{N_p} \sum_{i=1}^{N_p} e_d^{(i)} \tag{6}$$

where N_p = number of particles in the packing. Ideally, the probability density function (PDF) of e_d should be used to fully describe the distribution of the shape factor $\{e_d\}$. Yet, it is interesting to observe that the PDF of the normalized shape factor (e_d/E_d) follows a gamma distribution, which remains to be unchanged for samples under various loading stages. The detailed discussion will be presented in the Evolution of E_d and A_d section. Therefore, E_d becomes sufficient to describe the distribution of the shape factor $\{e_d\}$ in the entire packing.

Assume $\boldsymbol{n}$ is the unit vector along the principal orientation θ_d, then $(n_i, n_j) = (\cos\theta_d, \sin\theta_d)$ for the 2D case. Following the method proposed by Oda (1982), a fabric tensor can be defined as follows:

$$F_{ij} = \frac{1}{N_p} \sum_{k=1}^{N_p} n_i^{(k)} n_j^{(k)} = \oint_{\theta_d} f(\theta_d) n_i n_j d\theta_d \tag{7}$$

where $f(\theta_d)$ = angular distribution function of θ_d associated with all particles, i.e., $\oint_{\theta_d} f(\theta_d) d\theta_d = 1$. It can be approximated using a Fourier series as follows (Sitharam et al. 2009):

$$f(\theta_d) = f_0(1 + a_{ij} n_i n_j) \tag{8}$$

In the 2D case, $f_0 = 1/2\pi$ and a_{ij} is a symmetric second-order tensor that contributes to the deviatoric part of the fabric tensor, F'_{ij}, through the relationship $a_{ij} = 4F'_{ij}$. Eq. (8) can be expressed equivalently as

$$f(\theta_d) = \frac{1}{2\pi}[1 + |A_d| \cos 2(\theta_d - \Theta_d)] \tag{9}$$

where $|A_d| = [(a_{11} - a_{22})^2 + (a_{12} + a_{21})^2]^{1/2}/2$, which quantifies the anisotropy degree of $f(\theta_d)$; $\tan(2\Theta_d) = (a_{12} + a_{21})/(a_{11} - a_{22})$; and $\Theta_d \in (0, \pi)$ = principal direction of $f(\theta_d)$.

In this study, A_d is chosen as the second descriptor, named as the orientation-anisotropy descriptor, to quantify the particle-void distribution, and its absolute value measures the anisotropy of local void orientation. The sign of A_d is determined by Θ_d. When $\Theta_d \in (0, \pi/2)$, $A_d > 0$, and when $\Theta_d \in (\pi/2, \pi)$, $A_d < 0$.

The roles of E_d and A_d in the overall anisotropy of the packing are illustrated in Fig. 5. In the figure, the shaded shapes represent the local void distribution function $r(\theta)$ around different particles. Fig. 5(a) contains elongated shapes with random principle orientations. Obviously, the packing is overall isotropic, and it has a large value of E_d and a small value of $|A_d|$. On the other hand, Fig. 5(b) consists of elongated shape oriented in the same direction. Therefore, the packing is globally anisotropic, and has large values of E_d and $|A_d|$. As shown in Figs. 5(c and d), the shapes in Fig. 5(c) are randomly orientated, but along the same direction in Fig. 5(d). Yet, the differences between two patterns are not significant. Therefore, the overall anisotropy will be less affected by shape orientation if the shape is more spherical (i.e., small E_d).

Particle-Void Distribution before and after Liquefaction

Evolution of E_d and A_d

Until now, two descriptors, E_d and A_d, are derived from statistical analysis of shape factor $\{e_d\}$ and principal direction $\{\theta_d\}$ of $r(\theta)$ associated with all particles to quantify the particle-void distribution.

Firstly, the evolution of E_d and A_d during the whole loading process (before and after initial liquefaction) is examined. Figs. 6(a and b) demonstrate the evolution of E_d and A_d with the number of loading cycles under different CSRs. Note that before initial liquefaction, only the data at the end of each loading cycle are plotted. After initial liquefaction, more data points are presented to show the variation of E_d and A_d within each loading cycle. Loading path significantly influences the number of loading cycles for the sample to reach initial liquefaction, as shown in Fig. 6(a). For sample Dr = 46%, 345 loading cycles are required under CSR = 0.16 to reach initial liquefaction. When CSR increases to 0.18 and 0.20, the number of loading cycles decreases dramatically to 46 and 16, respectively. Interestingly, E_d and A_d have almost the same value ($E_d = 0.133$ and $A_d = 0.03$) for different CSRs at the initial liquefaction. It means that particle-void distribution at initial liquefaction is not influenced by different loading paths that lead the sample to liquefaction. The case of CSR = 0.16 in post-liquefaction is replotted in Figs. 6(c and d). Note that changes in both E_d and A_d are negligible before the initial liquefaction compared with that in the post-liquefaction stage.
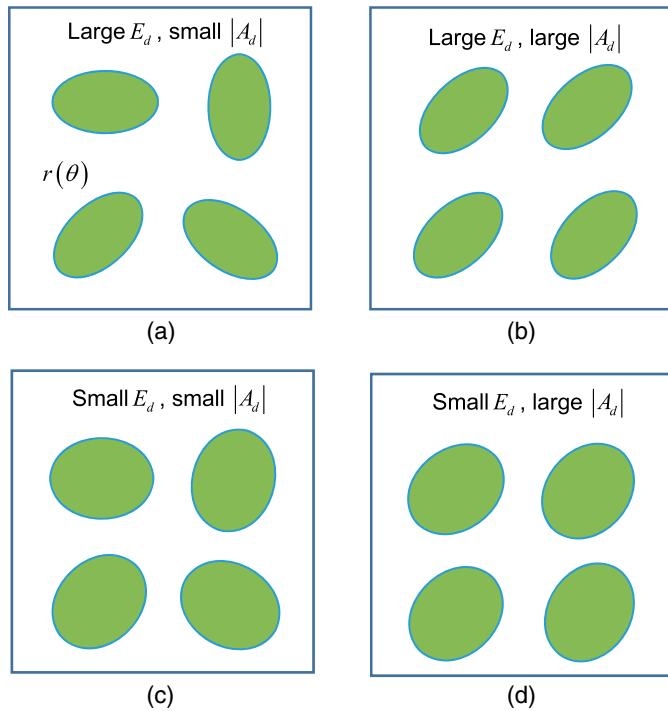
After initial liquefaction, the evolution of E_d and A_d gradually speed up as shown in Figs. 6(b and d). During the eight loading cycles after initial liquefaction, E_d decreases from 0.133 to 0.105 while the amplitude of A_d increases from 0.03 to 0.6. Afterwards, evolution of both E_d and A_d get stabilized. Within each loading cycle, E_d demonstrates alternative change from 0.105 to 0.117 and A_d varies from -0.6 to 0.6. It indicates the existence of an ultimate state in terms of particle-void distribution. The decrease in E_d means that local void distribution around a single particle (e_d) on average becomes less anisotropic. Fig. 7 shows the particle configuration and local void distribution at different stages. The line in each particle has the length of the particle diameter and tilts toward the orientation of θ_d. The thickness of the line measures the magnitude of e_d. Before initial liquefaction, large void space is found to distribute on one side of particles [refer to Fig. 7(a)], and the shape factor e_d associated with these particles has higher values. Continuous cyclic loadings will drive particle configuration toward to the packing in Fig. 7(b), in which local void is more uniformly (isotropically) distributed around particles. Consequently, shape factor e_d decreases.

Fig. 5. Schematic illustration of packings with different magnitudes of E_d and A_d.
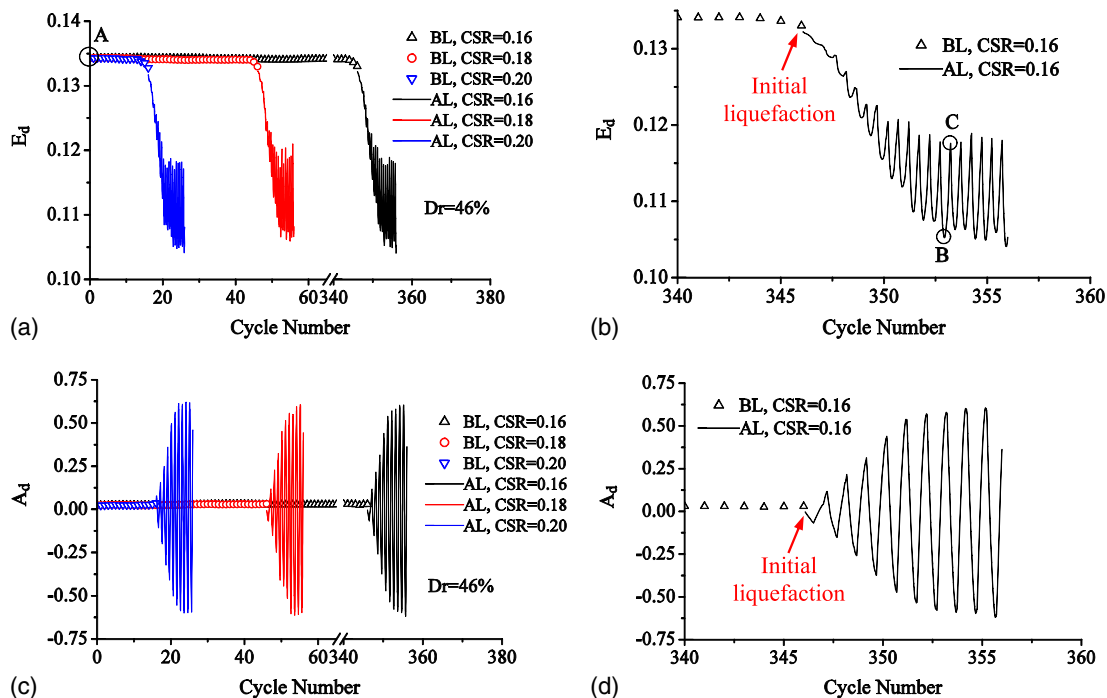
Fig. 6. Evolution of E_d and A_d with the number of loading cycles during the whole loading process. Data of E_d and A_d in post-liquefaction stage are enlarged in (b) and (d) for better illustration. In the legend, BL = before initial liquefaction and AL = after initial liquefaction.
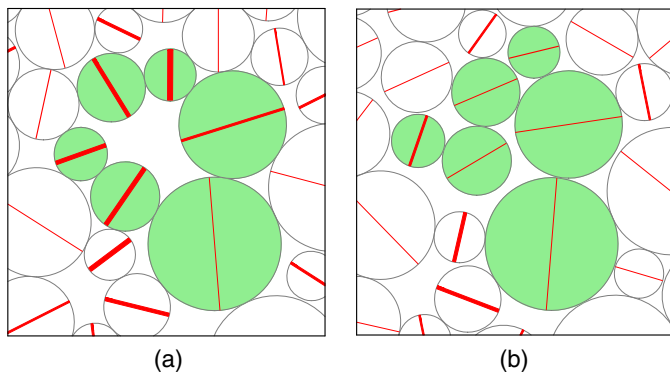
Fig. 7. Particle configuration and local void distribution of sample Dr46 at different stages: (a) before initial liquefaction ($E_d = 0.134$ and $A_d = 0.024$); and (b) after initial liquefaction ($E_d = 0.109$ and $A_d = 0.011$).

In the granular packing, e_d associated with all particles form a large data set with population of N_p (the number of particles). The mean value of e_d is denoted as E_d according to Eq. (6). It is interesting to notice that the PDF of the normalized variable, normalized e_d/E_d, remains unchanged at different loading stages. Fig. 8(a) demonstrates the PDF at three representative stages: Point A (the initial consolidation), Point B (the flow state in post-liquefaction), and Point C (the hardening state in post-liquefaction), as indicated in Figs. 6(a and b). The PDF of the normalized e_d/E_d can be well fitted by a single gamma distribution as follows:

$$P(x|a,b) = \frac{1}{b^a \Gamma(a)}(x)^{a-1} e^{-\frac{x}{b}} \quad (10)$$

where $x = e_d/E_d$; $\Gamma(a)$ = gamma function; $a = 1.688$ for all samples; and $b = 0.592$ for all samples. Moreover, the PDF of normalized e_d/E_d is found to be independent of relative densities of samples for the initial consolidation state, as demonstrated in Fig. 8(b). Therefore, only the mean value of e_d is sufficient as a descriptor to quantify the particle-void distribution.

Evolution of E_d and A_d within a Loading Cycle

Fig. 9 shows the evolution of E_d and A_d along with shear stress during a loading cycle (CSR = 0.16) in the post-liquefaction stage. Points 1–3 denote three typical states within an half loading cycle from $\tau = 16$ kPa to $\tau = -16$ kPa. Points 1 and 3 are selected at the

maximum shear stress where τ equals to 16 and -16 kPa, respectively. Point 2 is picked when $A_d = 0$ because the packing is under flow state with an effective stress of zero. A strong correlation among E_d, $|A_d|$, and shear stress can be clearly observed.

At Points 1 and 3 with the peak shear stress, both E_d and $|A_d|$ reach the peak value. At Point 2 ($A_d = 0$), E_d almost approaches its minimum value. Decrease of E_d during the unloading process (from Points 1 to 2) is due to the void redistribution during the collapse of load-bearing structure. As discussed previously, granular packing has higher value of E_d when the packing could sustain the load compared with the packing under the flow state (refer to Fig. 7). Upon reloading from Points 2 to 3, E_d increases as the load-bearing structure gradually establishes. Change of A_d from 0.54 in Point 1 to -0.53 in Point 3 can be explained by Fig. 10, which shows the θ_d associated with all particles in the sample and their angular distribution $f(\theta_d)$ at these three points. At the peak shear stress Points 1 and 3, θ_d associated with most particles is close to the extension direction, leading to a large value of $|A_d|$. On the other hand, at Point 2, θ_d is distributed isotropically along all directions, resulting in a small value of $|A_d|$.

Hardening State Line: Transition from Flow to Hardening State

In the post-liquefaction stage, granular packing will transform from a flow state to a hardening state under shearing, a phenomenon called *jamming transition* in the physics community. The transition point is defined to separate the flow strain (γ_0) and the hardening strain (γ_d) as shown in Fig. 1(d). To identify the transition points, coordination number Z, defined as the ratio between total interparticle contact number and total particle number ($Z = 2N_c/N_p$), can be used to differentiate the mechanical status of granular packing (Wang and Wei 2016; Wang et al. 2016). Fig. 11 demonstrates the evolution of Z during cyclic loading and the relation between Z and shear stress. Before liquefaction, Z gradually decreases from initial value of 3.36 to 2.2 at the initial liquefaction. With further cyclic loading in post-liquefaction, Z shows a strong variation within each loading cycle, where it drops to near zero at the flow state and increases to 2.4 at the hardening state. From Fig. 11(b), a strong correlation can be observed between Z and the shear stress such that the shear stress is negligible until Z is greater than a critical value of around 2. In other words, a particle on average needs at least two contacts from neighboring particles to establish a stable load-bearing structure in this sample. Similar observation can be made from the other two samples with different relative densities
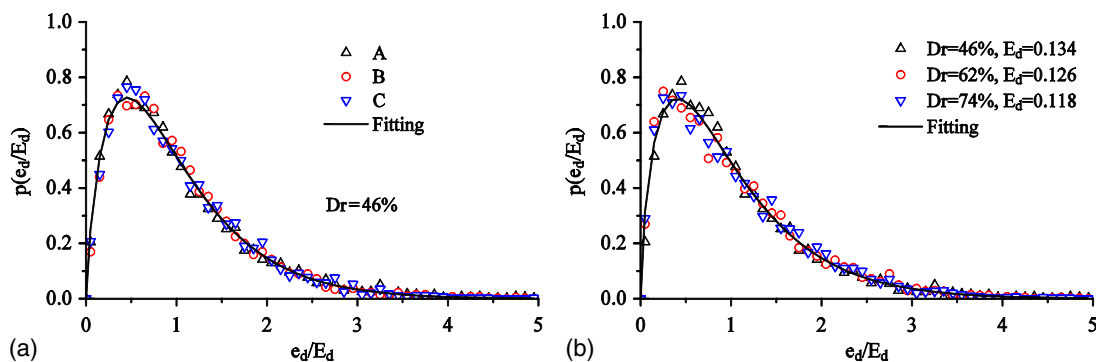
Fig. 8. (a) Probability distribution function of e_d/E_d for sample Dr = 46% at three loading stages; and (b) PDF of e_d/E_d for the three samples with different relative densities for the initial consolidation state. A, B, and C represent initial consolidation, flow state, and hardening state in post-liquefaction as shown in Figs. 6(a and b), respectively.
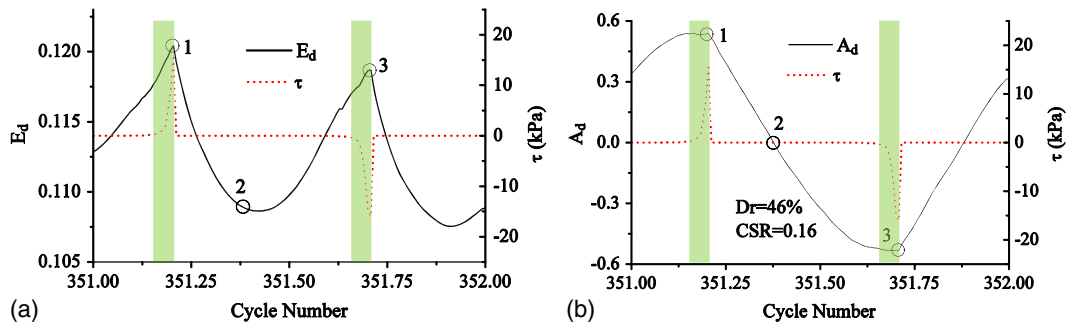
Fig. 9. Evolution of E_d and A_d within a loading cycle in the post-liquefaction stage: (a) the evolution of E_d; and (b) the evolution of A_d. Shear stress is also plotted for comparison.
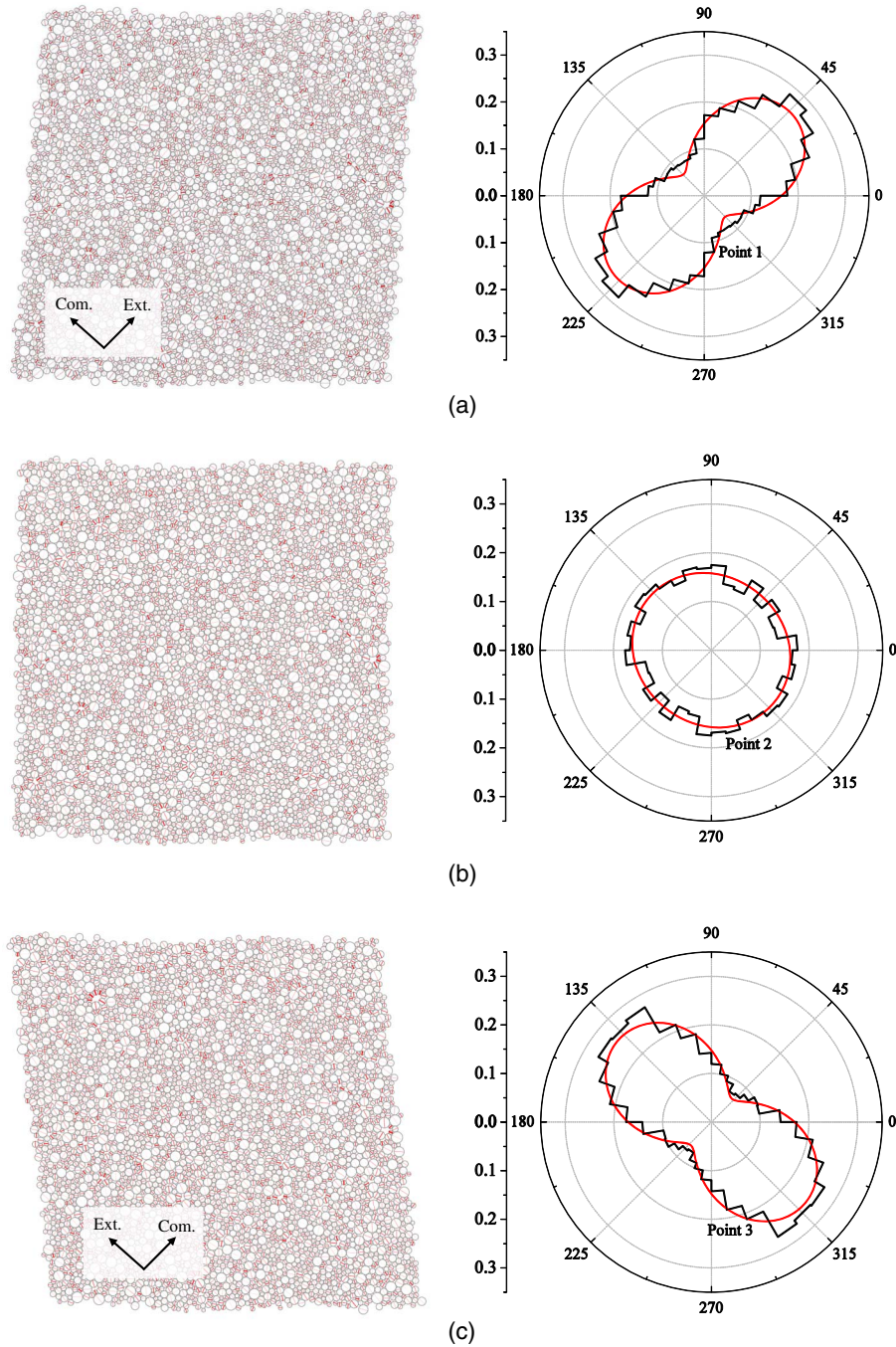
Fig. 10. Angular distribution $f(\theta_d)$ at three different stages (Points 1–3). The line in each particle has the length of the particle diameter and tilts toward the orientation of θ_d.
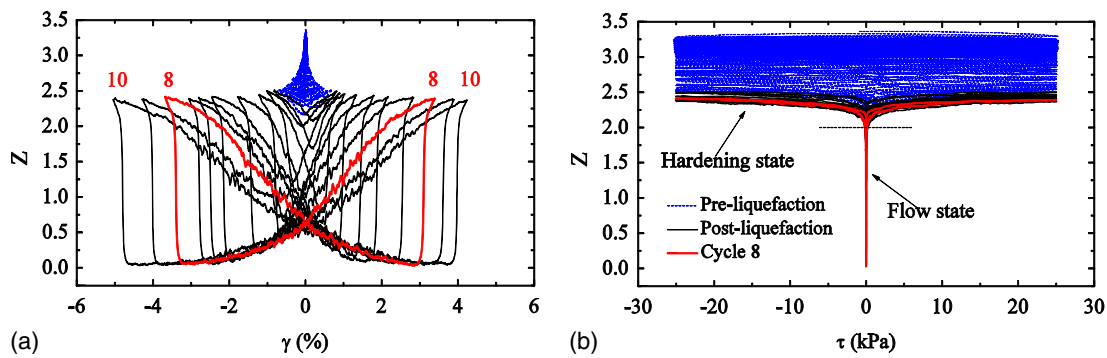
Fig. 11. Coordination number Z of sample $Dr = 62\%$ with $CSR = 0.25$. (a) Z versus strain curve; and (b) relation between Z and shear stress.
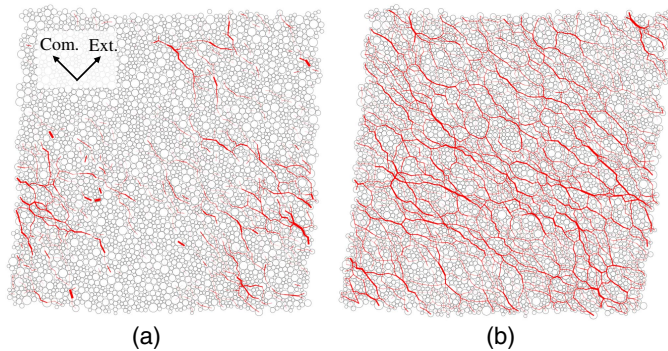
Fig. 12. Force chain network of sample $Dr = 62\%$: (a) $Z = 1$; and (b) $Z = 2$.

Fig. 13. (a) Evolution of E_d and A_d in the post-liquefaction stage (loading cycles after initial liquefaction are labeled) for $CSR = 0.25$, $Dr = 62\%$; and (b) hardening state lines (HSLs) for different CSRs.

($Dr = 46\%$ and $Dr = 74\%$). Therefore, $Z = 2$ is adopted to identify the jamming transition points.

The force chain network reflects how the stress is transmitted through the granular packing. Figs. 12(a and b) demonstrate the force chain network of sample $Dr = 62\%$ when $Z = 1$ and $Z = 2$. The thickness of the force chain denotes the magnitude of contact normal force. Note that the normal force of interparticle contacts is very small in both cases because the effective stress of the packing is almost zero. In the force chain network of $Z = 1$, most interparticle contacts distribute at two regions in the middle of the packing. The network is far from fully established. For the force chain network of $Z = 2$, the spatial distribution of interparticle contacts is more uniform. A preferred orientation of contact normals is clearly presented along the compression direction. Although the normal force of contacts is still very low, the network is fully established and provides a strong backbone for the further increase of effective stress and stiffness. The force chain network further confirms the identification of jamming transition point by $Z = 2$.

Fig. 13(a) shows the evolution of E_d and A_d during cyclic loading for sample $Dr = 62\%$. Given that the change in E_d and A_d is negligible before initial liquefaction, we only plot data in the post-liquefaction stage in Fig. 13(a). It can be observed that E_d decreases gradually with increasing of absolute A_d. Jamming transition point ($Z = 2$) and an intermediate point ($Z = 1$) are highlighted. It is worth mentioning that the jamming transition point clearly defines loci of a hardening state line (HSL) in the (E_d, A_d) plot. As can be seen in Fig. 13(a), an HSL can be approximately fitted by a linear equation. It delineates the boundary to separate the flow state and hardening state in the $E_d - A_d$ space. Inside HSL, granular packing belongs to the flow state with no load-bearing structure and behaves
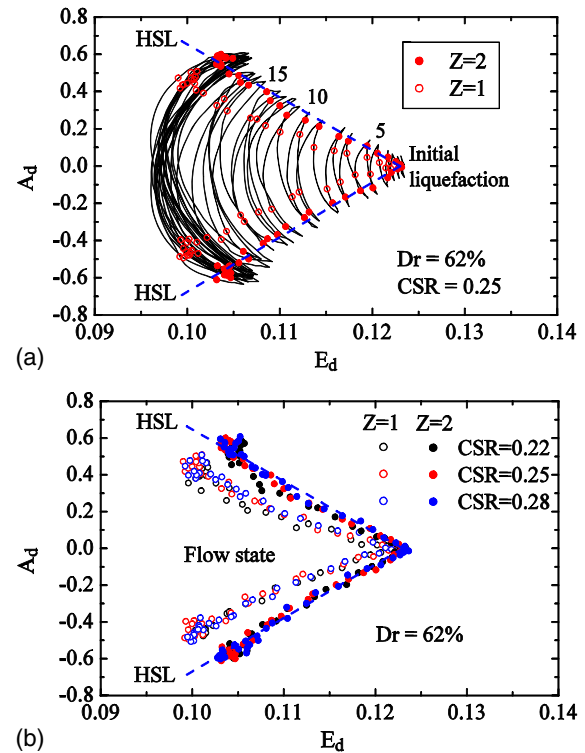
like a fluid. Beyond HSL, granular packing belongs to the hardening state with the stable load-bearing structure and behaves like a solid. The existence of HSL also indicates that the load-bearing structure in the post-liquefaction stage can be formed only if either E_d or $|A_d|$ becomes sufficiently large. Otherwise, the packing remains in a flow state.

Further, the uniqueness of HSL is examined using the same sample under cases with different cyclic stress ratios (CSRs) ($CSR = 0.22$, 0.25, and 0.28). As shown in Fig. 13(b), data from different loading cases are aligned on a single HSL, indicating that the particle-void distribution at the transition points is independent of different loading paths. Additionally, HSL is found to be influenced by relative densities of samples. As shown in Fig. 14, HSL shifts to the left for samples with higher density. On the other hand, the influence of relative density to the slope of the HSL is not significant based on the computational results.
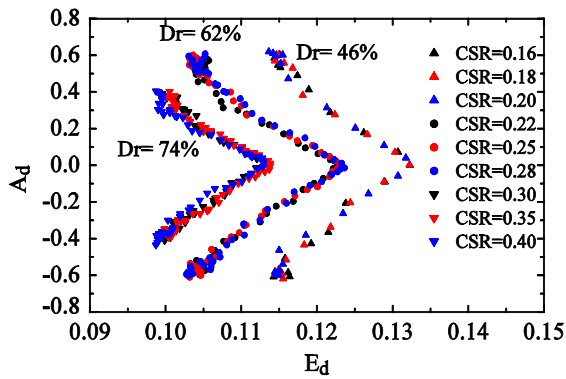
Fig. 14. HSL for different samples with different CSRs.
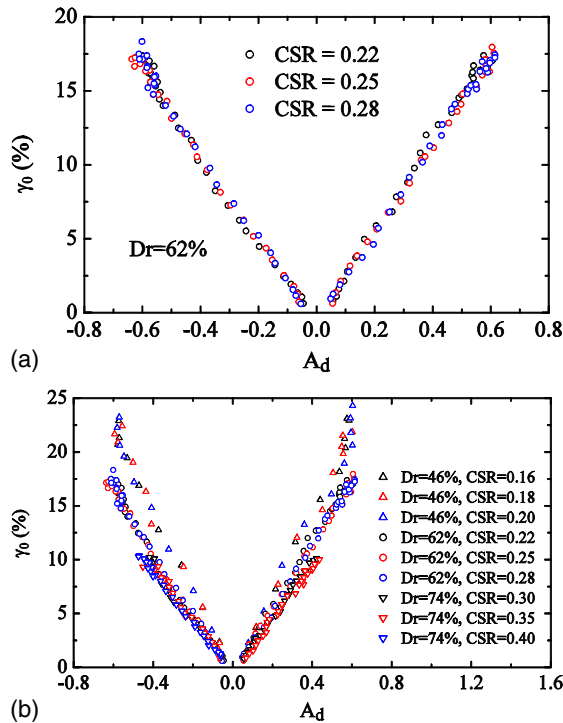
Fig. 15. (a) Relationship between A_d at the unloading points and the following flow strain amplitude (γ_0) with different loading paths; and (b) $A_d - \gamma_0$ relationship of samples with different relative densities.

Relationship between Flow Strain Amplitude and Particle-Void Distribution

For medium-to-dense sand, flow strain accumulates rapidly with the further loading cycles in the post-liquefaction stage, and this is referred as cyclic mobility. The flow strain amplitude in one cycle, denoted as γ_0 [refer to Fig. 1(d)], is the shear strain from the unloading point to the following jamming transition point. Fig. 15 presents the relationship between flow strain amplitude (γ_0) and the descriptor A_d, whose absolute value is chosen as the value at the previous unloading point. Fig 15(a) shows the $A_d - \gamma_0$ relation for the sample Dr = 62% under different loading paths. It can be observed that all data points are distributed along two well-defined symmetric lines. A strong correlation exists between the flow strain amplitude (γ_0) and $|A_d|$, indicating that a sample

with a higher $|A_d|$ at the unloading point will be followed by a larger flow strain (γ_0) to reach the next jamming state. Based on Fig. 15(a), the $A_d - \gamma_0$ relationship is not influenced by different loading conditions, given that the data points of different CSRs all follow the same trend. Fig. 15(b) shows the $A_d - \gamma_0$ curve of samples with different relative densities. The slope of the $A_d - \gamma_0$ curve becomes steeper and the maximum value of γ_0 is higher with decreasing relative density of samples. The maximum value of γ_0 at the ultimate state increases from 10% of sample Dr74 to 25% of sample Dr46.

Conclusions

In this study, new fabric measures, the shape-elongation descriptor E_d and the orientation-anisotropy descriptor A_d, for two-dimensional granular assemblies are developed to characterize the evolution of the particle-void fabric during cyclic liquefaction and cyclic mobility. It was observed that particle-void distribution of granular packing has no significant change before initial liquefaction. Different loading paths only affect the number of loading cycles leading the sample to initial liquefaction. The irreversible change in E_d and A_d is primarily developed in the post-liquefaction stage, in which the overall trend of the evolution is indicated by a gradual decrease of E_d and a gradual increase of $|A_d|$ cycle by cycle.

In the post-liquefaction stage, a hardening state line (HSL) can be defined in the $E_d - A_d$ space, which delineates the boundary to separate a flow state and a jamming state. The existence of an HSL indicates that jamming transition in liquefied soils, i.e., formation of a load-bearing structure, can only be possible if either E_d or $|A_d|$ becomes sufficiently large. A strong correlation is observed between $|A_d|$ and the post-liquefaction flow strain (γ_0). With a progressive increase of $|A_d|$ in the post liquefaction state, the flow strain (γ_0) is also progressively increasing until a stable particle-void state is reached. Interestingly, both the HSL and the $A_d - \gamma_0$ curve are unique and independent of loading paths for a packing.

Finally, it is worth mentioning that although the current study is based on two-dimensional DEM simulation, the work can be readily extended to three-dimensional assemblies. Such analysis will be conducted in the future on a greater range of simulations, including different types of tests, different initial anisotropy, and different particle shapes, to further verify the conclusions drawn in this study.

Acknowledgments

Notation

The following symbols are used in this paper:

A_d = descriptor for global anisotropy of local void orientation;

a, b = parameters in the gamma distribution;

Dr = relative density of granular sample;

E_d = descriptor for elongation of local void shape;

e = void ratio of granular sample;

e_{min}, e_{max} = minimum and maximum void ratio;

e_d = shape factor of local void distribution;

e_L = local void ratio;

$f(\theta_d)$ = angular distribution function of θ_d associated with all particles;

N_c = total number of interparticle contacts in the granular sample;

N_p = total number of particles in the granular sample;

$P^{(i)}$ = center of particle i;

$R^{(i)}$ = radius of particle i;

$R_c(\theta)$, $R_p(\theta)$ = radial dimension of the Voronoi cell and particle, respectively;

$r(\theta)$ = CP ratio, describes the distribution of the local void around a particle;

V_c, V_p = areas of the Voronoi cell and particle, respectively;

$[V_1^{(i)}, \ldots, V_k^{(i)}]$ = vertexes of the Voronoi cell associated with particle I;

Z = coordination number;

γ = shear strain;

γ_0 = flow strain in post-liquefaction stage;

γ_d = hardening strain in post-liquefaction stage;

θ_d = principal orientation of local void distribution;

Θ_d = principal direction of $f(\theta_d)$;

σ_v' = effective vertical stress;

$\sigma_{v,0}'$ = vertical consolidation stress; and

τ = shear stress.

References

Bowman, E. T., K. Soga, and W. Drummond. 2001. "Particle shape characterization using Fourier descriptor analysis." *Géotechnique* 51 (6): 545–554. https://doi.org/10.1680/geot.2001.51.6.545.

Chang, C. S., and Z. Y. Yin. 2010. "Micromechanical modeling for inherent anisotropy in granular materials." *J. Eng. Mech.* 136 (7): 830–839. https://doi.org/10.1061/(ASCE)EM.1943-7889.0000125.

Dafalias, Y. F., and M. T. Manzari. 2004. "Simple plasticity sand model accounting for fabric change effects." *J. Eng. Mech.* 130 (6): 622–634. https://doi.org/10.1061/(ASCE)0733-9399(2004)130:6(622).

Fonseca, J., C. O'Sullivan, M. R. Coop, and P. Lee. 2012. "Non-invasive characterization of particle morphology of natural sands." *Soils Found.* 52 (4): 712–722. https://doi.org/10.1016/j.sandf.2012.07.011.

Gao, Z., and J. Zhao. 2015. "Constitutive modeling of anisotropic sand behavior in monotonic and cyclic loading." *J. Eng. Mech.* 141 (8): 04015017. https://doi.org/10.1061/(ASCE)EM.1943-7889.0000907.

Ghedia, R., and C. O'Sullivan. 2012. "Quantifying void fabric using a scan-line approach." *Comput. Geotech.* 41 (Apr): 1–12. https://doi.org/10.1016/j.compgeo.2011.10.008.

Guo, N., and J. Zhao. 2013. "The signature of shear-induced anisotropy in granular media." *Comput. Geotech.* 47 (Jan): 1–15. https://doi.org/10.1016/j.compgeo.2012.07.002.

Guo, N., and J. Zhao. 2014. "Local fluctuations and spatial correlations in granular flows under constant-volume quasi-static shear." *Phys. Rev. E* 89 (4): 042208. https://doi.org/10.1103/PhysRevE.89.042208.

Idriss, I., and R. W. Boulanger. 2008. *Soil liquefaction during earthquakes. Monograph Series No. MNO-12*. Oakland, CA: Earthquake Engineering Research Institute.

Kuhn, M. R. 1999. "Structured deformation in granular materials." *Mech. Mater.* 31 (6): 407–429. https://doi.org/10.1016/S0167-6636(99)00010-1.

Li, X., and X. Li. 2009. "Micro-macro quantification of the internal structure of granular materials." *J. Eng. Mech.* 135 (7): 641–656. https://doi.org/10.1061/(ASCE)0733-9399(2009)135:7(641).

Mitchell, J., and K. Soga. 2005. *Fundamentals of soil behavior.* 3rd ed. New York, NY: Wiley.

Mollon, G., and J. Zhao. 2013. "Generating realistic 3D sand particles using Fourier descriptors." *Granul. Matter.* 15 (1): 95–108. https://doi.org/10.1007/s10035-012-0380-x.

Ng, T. T., and R. Dobry. 1994. "Numerical simulations of monotonic and cyclic loading of granular soil." *J. Geotech. Eng.* 120 (2): 388–403. https://doi.org/10.1061/(ASCE)0733-9410(1994)120:2(388).

Oda, M. 1982. "Fabric tensor for discontinuous geological materials." *Soils Found.* 22 (4): 96–108. https://doi.org/10.3208/sandf1972.22.4_96.

Oda, M., S. Nemat-Nasser, and J. Konishi. 1985. "Stress-induced anisotropy in granular masses." *Soils Found.* 25 (3): 85–97. https://doi.org/10.3208/sandf1972.25.3_85.

O'Sullivan, C. 2011. *Particulate discrete element modelling: A geomechanics perspective.* Oxon, UK: Spon Press.

O'Sullivan, C., J. D. Bray, and M. F. Riemer. 2002. "Influence of particle shape and surface friction variability on response of rod-shaped particulate media." *J. Eng. Mech.* 128 (11): 1182–1192. https://doi.org/10.1061/(ASCE)0733-9399(2002)128:11(1182).

Phusing, D., and K. Suzuki. 2015. "Cyclic behaviors of granular materials under generalized stress condition using DEM." *J. Eng. Mech.* 141 (10): 04015034. https://doi.org/10.1061/(ASCE)EM.1943-7889.0000921.

Pouliquen, O., M. Belzons, and M. Nicolas. 2003. "Fluctuating particle motion during shear induced granular compaction." *Phys. Rev. Lett.* 91 (1): 014301. https://doi.org/10.1103/PhysRevLett.91.014301.

Rothenburg, L., and R. Bathurst. 1989. "Analytical study of induced anisotropy in idealized granular materials." *Géotechnique* 39 (4): 601–614. https://doi.org/10.1680/geot.1989.39.4.601.

Satake, M. 1992. "A discrete-mechanical approach to granular materials." *Int. J. Eng. Sci.* 30 (10): 1525–1533. https://doi.org/10.1016/0020-7225(92)90162-A.

Seed, H. B., and K. L. Lee. 1966. "Liquefaction of saturated sands during cyclic loading." *J. Soil Mech. Found. Div.* 92 (6): 105–134.

Shamoto, Y., J. Zhang, and S. Goto. 1997. "Mechanism of large post-liquefaction deformation in saturated sand." *Soils Found.* 37 (2): 71–80. https://doi.org/10.3208/sandf.37.2_71.

Sitar, N. 1983. "Slope stability in coarse sediments." In *Special publication on geological environmental and soil properties*, edited by R. N. Yong, 82–98. Reston, VA: ASCE.

Sitharam, T., J. Vinod, and B. Ravishankar. 2009. "Post-liquefaction undrained monotonic behaviour of sands: Experiments and DEM simulations." *Géotechnique* 59 (9): 739–749. https://doi.org/10.1680/geot.7.00040.

Šmilauer, V., et al. 2015. "Using and programming." *In Yade documentation*, 2nd ed. https://doi:10.5281/zenodo.34043.

Thornton, C. 2000. "Numerical simulations of deviatoric shear deformation of granular media." *Géotechnique* 50 (1): 43–53. https://doi.org/10.1680/geot.2000.50.1.43.

Ventouras, K., and M. R. Coop. 2009. "On the behaviour of Thanet Sand: An example of an uncemented natural sand." *Géotechnique* 59 (9): 727–738. https://doi.org/10.1680/geot.7.00061.

Wang, G., and J. Wei. 2016. "Microstructure evolution of granular soils in cyclic mobility and post-liquefaction process." *Granul. Matter.* 18 (3): 51. https://doi.org/10.1007/s10035-016-0621-5.

Wang, G., and Y. Xie. 2014. "Modified bounding surface hypoplasticity model for sands under cyclic loading." *J. Eng. Mech.* 140 (1): 91–101. https://doi.org/10.1061/(ASCE)EM.1943-7889.0000654.

Wang, R., P. Fu, J. M. Zhang, and Y. F. Dafalias. 2016. "DEM study of fabric features governing undrained post-liquefaction shear deformation of sand." *Acta Geotech.* 11 (6): 1321–1337. https://doi.org/10.1007/s11440-016-0499-8.

Wang, Y. H., and C. M. Mok. 2008. "Mechanisms of small-strain shear-modulus anisotropy in soils." *J. Geotech. Geoenviron.* 134 (10): 1516–1530. https://doi.org/10.1061/(ASCE)1090-0241(2008)134:10(1516).

Wei, J., and G. Wang. 2015a. "Evolution of packing structure in cyclic mobility and post-liquefaction of granular soils." In *Bifurcation and degradation of geomaterials in the new millennium: Springer series in geomechanics and geoengineering*, edited by K. T. Chau and J. Zhao, 267–272. Hong Kong: Springer International Publishing.

Wei, J., and G. Wang. 2015b. "Microstructure evolution of granular soils during liquefaction process." In *Geomechanics from micro to macro*,

edited by K. Soga, K. Kumar, G. Biscontin, and M. Kuo, 251–256. London, UK: Taylor & Francis Group.

Wei, J., and G. Wang. 2016. "Evolution of fabric anisotropy in cyclic liquefaction of sands." *J. Micromech. Mol. Phys.* 1 (3/4): 1640005. https://doi.org/10.1142/S2424913016400051.

Wei, J., and G. Wang. 2017. "Discrete-element method analysis of initial fabric effects on pre- and post-liquefaction behavior of sands." *Géotech. Lett.* 7 (2): 161–166. https://doi.org/10.1680/jgele.16.00147.

Yimsiri, S., and K. Soga. 2010. "DEM analysis of soil fabric effects on behaviour of sand." *Géotechnique* 60 (6): 483–495. https://doi.org/10.1680/geot.2010.60.6.483.

Yin, Z. Y., C. S. Chang, and P. Y. Hicher. 2010. "Micromechanical modelling for effect of inherent anisotropy on cyclic behaviour of sand." *Int. J. Solids Struct.* 47 (14–15): 1933–1951. https://doi.org/10.1016/j.ijsolstr.2010.03.028.

Yin, Z. Y., P. Y. Hicher, C. Dano, and Y. F. Jin. 2017. "Modeling mechanical behavior of very coarse granular materials." *J. Eng. Mech.* 143 (1): C4016006. https://doi.org/10.1061/(ASCE)EM.1943-7889.0001059.

Zhang, G., and J. M. Zhang. 2008. "Unified modeling of monotonic and cyclic behavior of interface between structure and gravelly soil." *Soils Found.* 48 (2): 231–245. https://doi.org/10.3208/sandf.48.231.